Thermally actuated untethered impact-driven locomotive microdevices

O. J. Sul,[a)] M. R. Falvo,[b)] R. M. Taylor II,[b),c)] S. Washburn,[b),c),d)] and R. Superfine[b),c)]
Department of Physics and Astronomy, University of North Carolina at Chapel Hill, Chapel Hill, North Carolina 27599

The authors have developed steerable locomotive devices as small as 30 μm using the inertial impact drive as the thrust method. The devices consist of three-legged, thin-metal-film bimorphs designed to rest on three sharp tips with the device body curved up off the surface. Rapid, thermally induced curvature of one leg leads to stepwise translation on a low friction surface. A focused laser was used to supply energy and its parameters controlled the velocity and direction of motion of the device. © *2006 American Institute of Physics*. [DOI: 10.1063/1.2388135]

The convergence of robotics with microelectromechanical systems (MEMS) offers the promise of devices that can roam over space and perform tasks remotely.[1–4] Tasks such as the recovery and reconfiguration of micromaterials have been considered.[5] The strategy for movement over surfaces has included the gait of multiple legs,[6–10] the progressive motion through device deformation similar to crawling (scratch drive actuator),[11,12] and the motion caused by the rapid transfer of momentum from an isolated segment to the entire device, which we refer to as impulse drive.[13] In the smallest size ranges, these devices have ranged from the millimeter scale in the case of the impulse drive down to 200 μm for the scratch drive.[12] We have fabricated simple 30 μm devices that can roam over a surface using thermal energy. The localized heating by an external laser causes a rapid local deformation that propels the device across the surface. Through the use of a second laser beam to time resolve the local deformation of device structure, we identify the transport mechanism as impulse drive. We achieve velocities as large as 100 μm/s, step sizes as small as 30 nm and demonstrate the capability to steer the device.

The motility of a device that cycles through contraction and relaxation can be considered as one of two classes, an inchworm drive or an impulse drive. In the inchworm drive, a cyclic deformation results in the progressive forward motion of successive legs independent of the time scale of the deformation.[14] The second mechanism involves the generation of momentum and kinetic energy in the device that conveys the device forward.[13] During the contraction phase, the rapid motion of a part of the device generates kinetic energy. This energy is dissipated by the breaking of the adhesive contact and the sliding friction at the contacts of the device over the surface. Essentially all of the forward motions are accomplished by the end of a contraction phase; in the remaining relaxation phase the device returns to its original shape. Both mechanisms must overcome stiction. For impulse drive, the device performance will be better at a low friction substrate such as highly oriented pyrolytic graphite (HOPG) (Fig. 1). The time scale of the deformation is critical to its motion as slow motions do not generate enough kinetic

energy to break the adhesive contact to the surface or generate significant sliding.

For steering, asymmetry in the device response and between the contraction and relaxation phases must be understood. If the device response is spatially symmetric in a contraction phase, the device will not move. If the response is symmetric between contraction and relaxation, any forward motion accomplished in one phase would be offset by an equivalent backward motion in the other phase. During the contraction phase in our devices [Fig. 2(a)], the fast temperature change and hence deformation are predominant in the one leg where energy is deposited. During the retraction phase, the heat has spread throughout the device and so the shape deformation is symmetric about the device center. Time asymmetry is provided by the different thermal profiles during the two phases. The contraction of this illuminated leg causes the surface contact of that leg to slide on the surface, while the counterbalancing force is applied by the other *two* contact spots. This spatial asymmetry allows the back (illuminated) leg to slide forward while the front two contact points remain relatively still.

We can gain important insight into the mechanism of an impulse-drive device by setting the kinetic energy generated in the excitation to the energy dissipated by the release of the contacts and sliding friction. If we assume our device is a one-dimensional arc, the movement of the center of mass is half of the deflection D of one of the legs. A velocity of the center of mass obtained by the device will be given simply by $D/2\Delta t$, where Δt is the time for the mechanical contraction, which leads to an energy balance equation,

$$\frac{mD^2}{8\Delta t^2} = f_{\text{dynamic}}l + f_{\text{stiction}}a, \tag{1}$$

where l is a slide distance, m is the device mass, and a is a contact diameter. We have performed finite element analysis (FEA, FEMLAB, Comsol Inc.) simulations on the spatiotem-
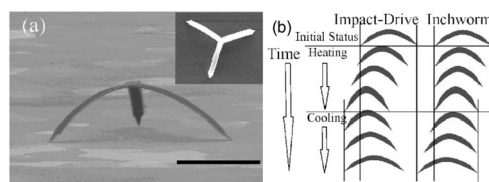

FIG. 1. (a) Angled SEM image of a device standing on the HOPG. The scale bar is 20 μm long (inset: top view). (b) Comparison of idealized drawing of the essential features of an impulse drive and inchworm walk that move through the successive deformations of the device.

a)Electronic mail: ojsul@physics.unc.edu
b)Also at Curriculum in Applied and Materials Sciences, University of North Carolina at Chapel Hill, Chapel Hill, NC 27599.
c)Also at Department of Computer Science, University of North Carolina at Chapel Hill, Chapel Hill, NC 27599.
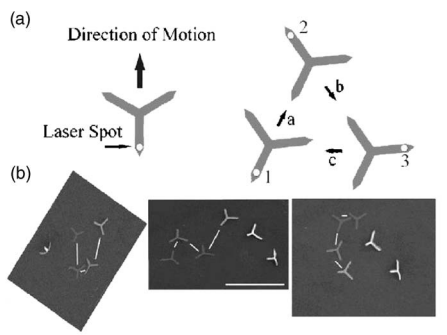d)Also at Deptartment Biomedical Engineering, University of North Carolina at Chapel Hill, Chapel Hill, NC 27599.

FIG. 2. Schematic of asymmetric driving and steering demonstration with initials "U," "N," and "C." (a) If L1 laser is set on location 1 (2 or 3), the device moves in *a* (*b* or *c*) direction. (b) In the top down SEM pictures, other stationary devices are landmarks. The scale bar is 120 μm.

FIG. 3. Optics diagram to actuate and to monitor the motions.

poral temperature profile and shape deformation of our devices, the full results of which are outside the scope of this letter and will be reported elsewhere.[15] These simulations show a linear dependence of the device deflection on the laser power. An equilibrium temperature increased linearly to the power absorbed if the laser pulse is longer than the natural contraction/relaxation time of a device. As expected from the distortion of a bilayer beam,[16] the deflection was proportional to the temperature. We can then write $D = CP$, where C is a constant that depends on the device geometry and the two material elastic properties, and P is the absorbed laser power. From the FEA results,[15] we calculate that $C = 63$ nm/mW for 15 μm device and 120 nm/mW for 25 μm device. Then Eq. (1) can be rearranged,

$$l = \frac{1}{f_{\text{dynamic}}} \left(\frac{mC^2}{8\Delta t^2} P^2 - f_{\text{stiction}} a \right). \tag{2}$$

From this model we draw several conclusions. First, a threshold laser power is required to overcome stiction and to initiate motion. Second, the slide distance will be increased by a decrease in the sliding friction. This guided our choice of graphite as the substrate. Most importantly, the slide distance is proportional to the square of the laser power. This is a feature of the impactdrive, where the kinetic energy is responsible for the motion. An inchworm drive would have a step length linearly proportional to the leg deformation, and hence, be linear in the laser power P.

We have designed our devices to be simple enough to display locomotion while retaining the steering capability. Because stiction is a major impediment, our three-legged devices have most of their body up off the surface and are supported by lithographically defined point contacts. To fabricate such a device, we used the intrinsic stress of an Al:Cr bilayer. The radial spokes were drawn on a polymethyl methacrylate layer on SiO_2 with electron-beam lithography. A thermal evaporator deposited 5 nm of Au, 400 nm of Al, and 200 nm of Cr. We used reactive ion etching (RIE, Samco Inc.) to remove the oxide layer everywhere except under the metal. Although RIE did not etch the oxide underneath the spokes, it could separate them and make the center of the spokes barely held at the oxide. The substrates were covered by a freshly cleaved HOPG sample. Due to the van der Waals and capillary forces, the devices were transferred onto the HOPG. About 1/3 of peeled devices arrived safely at the HOPG substrate with an overall transfer rate of roughly 10%.

The energy was supplied by a diode laser (L1: DL7147-201, Thorlabs, Inc., Fig. 3) focused to an adjustable 20 mW,
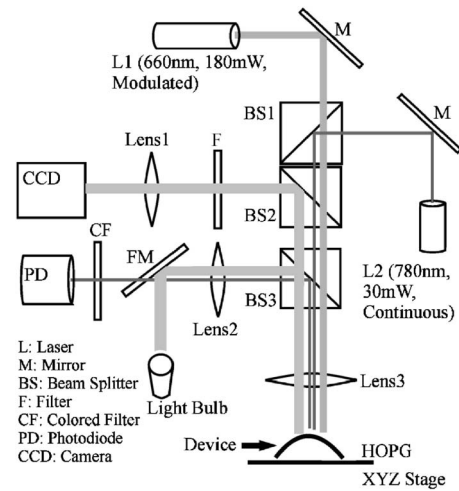
3 μm spot at a device by an objective lens (Lens3). A charge-coupled device (CCD) camera monitored the device motion and laser alignment. As soon as the laser spot was focused on the device, it roamed over the substrate in the focal plane (*XY* direction). High speed device deformation and motion were monitored by the reflection of a second laser (L2: L805P100, Thorlabs, Inc.) focused to a 2 mW, 3 μm spot by the same objective lens with microsecond resolution on a 300 MHz oscilloscope. The reflection of the L2 was filtered and directed to a photodiode. The amount of the reflection depended on the local angle of the device surface, which in turn was a function of three factors: (1) temporal deformations of the devices, (2) location of the L2 focal spot on the back of devices, and (3) net translation of the devices. The reflected signal was calibrated for the location on the device and the local angle by translating the beam over a stationary device and comparing this signal with the geometry of the device as measured by scanning electron microscope (SEM) images.

The device was observed to move across the surface only when specific criteria were satisfied. First, the heating laser had to be directed onto one of the legs. The velocity was zero with obvious symmetric shape deformation when the heating laser was on the center of the device, and rose steadily as the laser spot moved toward the end of the device leg. The heating laser needed to be pulsed: a continuous beam generated no motion, and the velocity dependence on pulse frequency was measured at constant pulse width and instantaneous power. For example, the step size was 450±200 nm for a 175±20 μs pulse width, 18±1 mW power, and at the 50 Hz frequency, dropping to 30±20 nm at 2 kHz, with motion ceasing above 5 kHz. The values for the step size were in quantitative accord with our FEA simulations, and the pulse frequency dependence was in agreement with the calculated and measured thermal relaxation time of the devices. At the highest frequencies, the device does not have time to cool and to recover its original shape before the next heating pulse comes along.

Figure 4(a) shows the two sets of five cycles of time resolved reflection of the L2 during the heating and cooling phases. Trace (A) shows the signal returning to its original base line, consistent with the device returning to its original shape and location. Trace (B) reveals the device's stepping forward on each laser pulse with a net translation after each
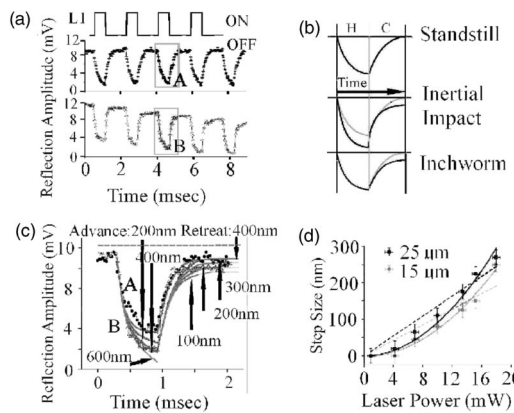
FIG. 4. (a) Wave forms of L2 reflections during pulsed heating by L1. Sequences recorded while the device was not translating (A) and translating (B). (b) Comparison of two simplified models of device motion. Both mechanisms are compared with the signal from a stationary device where the heated leg moves during heating (H) and returns to the original position during cooling (C). (c) Comparison between cycles from A and B in (a). The smooth curves are FEA simulations of device deformatioin. (d) Average step size for two different sized devices as a function of L1 power. The dotted and solid lines represent linear and quadratic fits (forced through the origin).

cooling phase. We consider how the temporal traces reveal details of the device motion. If the front legs are pinned, and the back leg illuminated, the heated leg would bend with its tip translating, but return to the same position upon cooling [Fig. 4(b)]. For an impulse driven device, net translation occurs during the heating phase with relaxation in the cooling phase. The inchworm mechanism would have the net forward motion during the cooling phase. We compared the reflection signal for a translating device with one where the front legs of the three legged device are pinned against a substrate step [Fig. 4(c), traces (A) and (B)]. The free device is observed to translate during the heating phase, with a significant decrease in the bias level in comparison with that of the pinned device.

Further insight is gained by the dependence of the step size on the L1 pulse energy, which we measure through a change in the instantaneous laser power at fixed pulse width of 380 μs, 500 Hz repetition rate. Movements of devices were recorded with the CCD camera with 1 μm resolution. A home-built tracking software[17] followed background illumination on the devices (obviously separate from laser spots) in the digital frames as location tags to determine the location of the devices. Our system had no automated tracking method. Therefore, as the device translates across the sample, the laser spot moves on the leg of the spider and finally off the device. We record the highest speed during this motion. After speed measurements, the values were divided by the driving frequency to get the step sizes. We plot the measured step length dependence on the laser power in Fig. 4(d) for 25 and 15 μm devices.

A threshold power for translation is observed with an increasing step size. While a power law is difficult to assess for data spanning one decade, we compare linear and quadratic fits. The square law fits capture the rapid rise of the step length as the laser power is increased, consistent with impulse driven devices. Equation (2) was fitted to each data set to estimate the stiction, $f_{stiction} = 20 \pm 10$ and 25 ± 10 pN, respectively, for 15 and 25 μm devices, and $f_{dynamic} = 10 \pm 5$ and 25 ± 10 pN, respectively. When $f_{dynamic}$ is divided by an estimated total contact area of 27 nm^2 of a device,[18] the shear stress of the HOPG can be calculated as 0.4 ± 0.2 and

0.9 ± 0.4 MPa. The results are comparable to shear stress measurements on other carbon materials, 2 MPa.[19]

Attempts to drive 5 μm devices failed for all laser parameters. From these experiments and from FEA analysis we infer that, for a given device thickness, driving laser spot size, and material choice, there will be a minimum device size that can achieve translation. Fundamentally, there is a competition between the thermal relaxation and the mechanical actuation time scales. For a device that is small enough, the thermal profile becomes homogeneous before the device can flex locally, and the flexure becomes uniform throughout the device instead of being localized to one leg, and hence, locomotion ceases below this size. The size limit might change if we were to load the devices with cargo. The cargo would provide extra thermal mass that would alter the time constant to reach equilibrium. Depending on the position of the cargo, the size limit might grow or shrink. The only other effects of cargo that we foresee are changes in the stiction amplitude and, of course, added mass, and both of these effects appear in straightforward ways in Eq. (2).

We have demonstrated the remote control of steerable freestanding MEMS structures as small as 30 μm over a surface with energy supplied by a laser. Through detailed time resolved measurements of shape deformation and device translation, we have determined that the motility mechanism is that of an impulse drive.

[1] P. Basset, A. Kaiser, P. Bigotte, D. Collard, and L. Buchaillot, Proceedings of the 15th International Conference on Microelectromechanical Systems, Las Vegas, 2002 (unpublished).

[2] H. Miura, T. Yasuda, Y. K. Fujisawa, and I. Shimoyama, Proceedings of the Transducers '95, Eurosensors IX; The 8th International Conference on Solid-State Sensors and Actuators, Stockholm, Sweden, 1995 (unpublished).

[3] K. Suzuki, I. Shimoyama, and H. Miura, J. Microelectromech. Syst. **3**, 4 (1994).

[4] R. Yeh, E. J. J. Kruglick, and K. S. J. Pister, J. Microelectromech. Syst. **5**, 10 (1996).

[5] P. Dariot, R. Valleggi, M. C. Carrozza, M. C. Montesi, and M. Cocco, J. Micromech. Microeng. **2**, 141 (1992).

[6] T. Ebefors, J. U. Mattsson, and E. Kalvesten, J. Micromech. Microeng. **10**, 337 (2000).

[7] T. Ebefors, J. U. Mattsson, E. Kalvesten, and G. Gtemme, *10th International Conference on Solid-State Sensors and Actuators (Transducers '99)*, Sendai, Japan, 1999.

[8] P. E. Kladitis and V. M. Bright, Sens. Actuators, A **80**, 132 (2000).

[9] M. H. Mohebbi, M. L. Terry, and K. F. Bohringer, *Proceedings of the 2001 ASME International Mechanical Engineering Congress and Exposition* (ASME, New York, 2001).

[10] S. Baglio, S. Castorina, L. Fortuna, and N. Savalli, *Proceedings of the IEEE International Symposium on Circuits and Systems*, Phoenix (IEEE, New York, 2002), Pt. 4 IV-285.

[11] T. Akiyama and K. Shono, J. Microelectromech. Syst. **2**, 106 (1993).

[12] B. R. Donald, C. G. Levey, C. D. McGray, D. Rus, and I. Paprotny, J. Microelectromech. Syst. **15**, 1 (2006).

[13] O. Ohmichi, Yamagata, and T. Higuchi, J. Microelectromech. Syst. **6**, 200 (1997).

[14] M. P. de Boer, D. L. Luck, W. R. Ashurst, R. Maboudian, A. D. Corwin, J. A. Walraven, and J. M. Redmond, J. Microelectromech. Syst. **13**, 63 (2004).

[15] O. J. Sul, Thesis, University of North Cardina at Chapel Hill, 2006.

[16] G. A. Gehring, M. D. Cooke, I. S. Gregory, W. J. Karl, and R. Watts, Smart Mater. Struct. **9**, 918 (2000).

[17] Check the website for more information on the tracking software at http://www.cs.unc.edu/Research/nano/cismm/download/spottracker/video_spot_tracker.html

[18] B. V. Derjaguin, V. M. Muller, and Y. P. Toropov, J. Colloid Interface Sci. **53**, 314 (1975).

[19] M. Falvo, R. M. Taylor II, A. Helser, V. Chi, F. P. Brooks, Jr., S. Washburn, and R. Superfine, Nature (London) **397**, 236 (1999).